

Numerical correction of anti-symmetric aberrations in single HRTEM images

Ossi Lehtinen¹, Dorin Geiger¹, Zhongbo Lee¹, Michael B. Whitwick², Ming-Wei Chen², Andras Kis², and Ute Kaiser¹

¹Central Facility for Electron Microscopy, Group of Electron Microscopy of Materials Science, University of Ulm, 89081 Ulm, Germany

²Electrical Engineering Institute, Ecole Polytechnique Federale de Lausanne (EPFL), CH-1015 Lausanne, Switzerland

December 6, 2024

Abstract

Here, we present a numerical post-processing method for removing the effect of anti-symmetric residual aberrations in high-resolution transmission electron microscopy (HRTEM) images of weak scattering objects. The method is based on applying the same aberrations with the opposite phase to the Fourier transform of the recorded image intensity and subsequently inverting the Fourier transform. We present the theoretical justification of the method and its verification based on simulated images. Ultimately the method is applied to experimental hardware aberration corrected HRTEM images resulting in images with strongly reduced residual aberrations, and consequently improved interpretability. Alternatively, this method can be used to measure accurately residual anti-symmetric aberrations in HRTEM images.

1 Introduction

Thanks to the practical realization of hardware aberration correction (AC), the point resolution of high-resolution transmission electron microscopy (HRTEM) is not limited by the positive spherical aberration any longer [1, 2, 3], and materials can now be routinely imaged at atomic resolution with state-of-the-art instruments even at low acceleration voltages [4, 5]. Once the strong C_s contribution is removed, other aberrations such as three-fold astigmatism (A_2), and coma (B_2) become measurable and can be corrected [3] down to a limit imposed by the measurement accuracy and the adjustment precision of the correcting elements. With advanced techniques, such as electron holography [6, 7, 8] and

exit wave reconstruction from a focal series [9, 10, 11, 12, 13] direct information on the specimen, not obscured by the inevitable residual aberrations, can be acquired. However, these techniques require special arrangements/procedures during the acquisition of the images, and thus cannot be applied to a single HRTEM image *post-situ*.

The wave aberrations distort the information transferred from the specimen to the imaging device, such as a CCD camera, making interpretation of the acquired images difficult if not sometimes impossible [14]. In a corrected microscope this problem is to a large extent overcome, as is evident from the nearly aberration free images of today. In the context of this article, the word *nearly* should be emphasized, however. The aberration coefficients can be tuned down to zero only with some accuracy. Thus, in practice residual aberrations are always present even in corrected instruments [15, 16]. Moreover, the instruments tend to drift away from the corrected state over time, and one can expect stronger residual aberrations as time passes after tuning the corrector. Residual aberrations can be also of benefit, like in the case of C_s , as non-zero C_s is required for optimal phase contrast transfer [3].

On the other hand, residual aberrations such as A_2 and B_2 , which can be present in the order of 100 nm after correction, can lead to undesired artefacts in the images, and the effect of these can be anything from a minor nuisance to complete misinterpretation of the image. Examples of such effects are presented in Figure 1. In the first panel, an AC-HRTEM image of a point defect in single-layer graphene can be seen. The presence of residual aberrations in the image is clear from the strongly non-hexagonal appearance of the graphene lattice. This effect can be attributed to the three-fold astigmatism A_2 , which has three axes of symmetry in the image plane (see Figure 1c for a visualization): Depending on the relative orientation of A_2 to the graphene lattice, one of the two sublattices of graphene can produce a higher contrast than the other, resulting in the observed non-hexagonal pattern. The atomic structure of the defect can still be deduced from the experimental image, but the image is far from optimal.

In the second panel, an AC-HRTEM image of so-called mirror-twin-boundaries in a single-layer MoSe_2 sample can be seen. In an aberration-free image the Se sites produce higher contrast as compared to the Mo sites, as there are always two Se ($Z=34$) atoms at the same location as opposed to single Mo ($Z=42$) atoms. However, in the recorded image the lattice has a completely different appearance at the different sides of the linear boundaries. On one side the second sublattice has a much higher contrast, but on the other side the sublattices have almost equal contrast, resulting in the hexagonal appearance of the lattice. This effect can again be attributed to residual A_2 , which is oriented matching the sublattices of the crystal with trigonal symmetry (see Figure 1 panel c). On one side of the boundary the Se sites are further enhanced, increasing the contrast difference of the Mo and Se sites. However, when crossing the boundary, the Mo and Se sites are interchanged (see Figure 1 panel d), and now the A_2 has the effect of reducing the contrast difference resulting in nearly equal contrast for the Mo and Se sites. Evaluation of the contrast could lead one to deduce that there are two different materials on the opposite sides of the boundary,

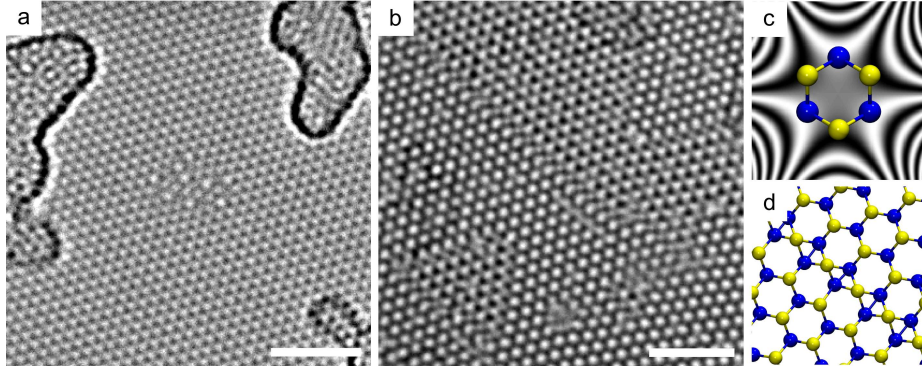


Figure 1: **AC-HRTEM images of graphene and MoSe₂ suffering from residual aberrations.** **a:** A defect structure in single-layer graphene, where the graphene lattice does not appear hexagonal due to residual aberrations. This effect can be attributed to residual three-fold astigmatism (A_2), which induces a contrast difference between the sublattices of graphene, causing the lattice image to deviate from the hexagonal symmetric pattern expected for graphene. **b:** Mirror-twin-boundaries in single-layer MoSe₂. Due to residual aberrations, the lattice has a completely different appearance on the opposite sides of the boundaries. Also this effect can be explained by alignment of the MoSe₂ lattice with residual A_2 (panel **c**) and by the swapping of the Mo and dual Se sites in the three-fold symmetric lattice when crossing the boundary (see panel **d** for the structure, where the dark atoms represent Mo and light atoms Se, with two Se atoms always residing on top of each other). The reversal of the lattice results in the accentuation of different sublattices in these regions. The scale bars are 2 nm.

which in fact is not the case! We would like to emphasize that these artefacts are not introduced by exceptionally strong residual aberrations. Under our experimental conditions, the A_2 coefficient is in the order of 100 nm, which is a typical state of correction after tuning in our microscope (FEI Titan 80-300, operated at 80 kV).

As mentioned above, numerous methods for acquiring truly aberration-free images in TEM have been proposed and implemented in practice. The common denominator of these methods is that they aim at recovering the object wave function, which then can be manipulated much more freely and interpreted more directly than a simple intensity image [17, 8, 11, 12, 13]. In electron holography [6, 7], an interference pattern between the object wave and a reference wave is generated with the help of a bi-prism, and direct information on the object wave can be recovered numerically from this pattern. The C_s corrector improves the phase-detection limit of electron holography significantly [8]. Another group of methods is in-line holography, *i.e.*, exit wave reconstruction [18, 9, 10, 11, 12, 13], where typically a series of images at equally spaced foci is acquired and subsequently the object wave is deduced iteratively. After the 'raw' electron wave is recovered, the influence of any residual aberrations can be corrected [17, 8]. A common drawback of these methods, however, is that they all require special arrangements and/or procedures during acquisition of the images, and hence cannot be applied to a single HRTEM image during post-processing. Such a situation can be quite frustrating if the microscopist has managed to capture an elusive target during imaging, but the resulting image is of poor quality.

Here, we present a method for numerically removing the effects of a specific group of geometric aberrations (the anti-symmetric ones, as discussed later) in HRTEM images *after* acquisition in single images. The method bears strong resemblance to exit wave reconstruction from focal series, but instead of going all the way to reconstructing the exit wave from a stack of images, we remove the contribution of residual aberrations in the fast Fourier transform (FFT) of a single image and transform it back to an image with corrected anti-symmetric aberrations. We want to make clear, that the effect of the symmetric aberrations, such as defocus or C_s cannot be remedied by our method. This is clear already from the fact that the symmetric aberrations lead to loss of information at certain frequencies (the zero crossing points of the contrast transfer function), which of course cannot be recovered. We find our method to be particularly useful for removing the effects of residual aberrations in distorted AC-HRTEM images where information is available on how the image *should* look like, as demonstrated with the examples of graphene and MoSe₂.

2 Methods

First, we present the theoretical background and justification of our method. We follow closely the notation of Ref. [19].

Assuming coherent illumination, the wave function $\Psi_z(\mathbf{x})$ at the image plane at a distance z from the object along the optical axis can be written as

$$\Psi_z(\mathbf{x}) = \Psi_0(\mathbf{x}) \otimes p_z(\mathbf{x}) = (1 + \phi(\mathbf{x})) \otimes p_z(\mathbf{x}), \quad (1)$$

where $\Psi_0(\mathbf{x})$ is the wave at the exit surface, $\phi(\mathbf{x})$ is the scattered wave, $p_z(\mathbf{x})$ is the lens transfer function and \otimes denotes convolution. At this point we have made no assumptions about the scattered wave other than that it is a complex valued function. The image intensity $i_z(\mathbf{x})$ is the square modulus of the wave at the detector plane, and its Fourier transform $I_z(\mathbf{u})$ can be written as

$$\begin{aligned} I_z(\mathbf{u}) &\equiv \mathcal{F}\{\Psi_z \cdot \Psi_z^*\} \\ &= \mathcal{F}\{1 + \phi \otimes p_z + \phi^* \otimes p_z^* + (\phi \otimes p_z)(\phi^* \otimes p_z^*)\} \\ &\approx \delta(\mathbf{u}) + \Phi(\mathbf{u}) \cdot e^{i\chi(\mathbf{u})} + \Phi^*(-\mathbf{u}) \cdot e^{-i\chi(-\mathbf{u})}, \end{aligned} \quad (2)$$

where $\Phi(\mathbf{u})$ denotes the Fourier transform of $\phi(\mathbf{x})$. The Fourier transform of p_z is written in the explicit form $e^{i\chi(\mathbf{u})}$. The information about the microscope aberrations are encoded in the wave aberration function $\chi(\mathbf{u})$, and we will return to it shortly. Meanwhile, it is important to note, that here the first approximation has been made, that is, the last term on the second line of the equation is deemed to be small, which is the case for a weak scattering object [19].

Now, $\chi(\mathbf{u})$ can be represented as a power series where each term represents a specific aberration. The terms of the series can be divided into symmetric $\chi_s(\mathbf{u}) = \chi_s(-\mathbf{u})$ and anti-symmetric $\chi_{as}(\mathbf{u}) = -\chi_{as}(-\mathbf{u})$ parts. Notably, the defocus and C_s belong to the symmetric group and A_2 and B_2 to the anti-symmetric group. Thus, $I_z(\mathbf{u})$ can be written as

$$I_z(\mathbf{u}) = \delta(\mathbf{u}) + \Phi(\mathbf{u}) \cdot e^{i\chi_s(\mathbf{u})} e^{i\chi_{as}(\mathbf{u})} + \Phi^*(-\mathbf{u}) \cdot e^{-i\chi_s(\mathbf{u})} e^{i\chi_{as}(\mathbf{u})}. \quad (3)$$

From this equation it is evident, that the effect of the *anti-symmetric* aberrations can be removed from the image by simply multiplying $I_z(\mathbf{u})$ by $e^{-i\chi_{as}(\mathbf{u})}$ and calculating the inverse Fourier transform. That is, a corrected image $i_c(\mathbf{x})$ can be generated by

$$i_c(\mathbf{x}) = |\mathcal{F}^{-1}\{e^{-i\chi_{as}(\mathbf{u})} \cdot \mathcal{F}\{i_z(\mathbf{x})\}\}|. \quad (4)$$

It should be emphasized, however, that prior knowledge of the aberration coefficients is required for conducting the correction. Information on the residual aberrations is offered by the corrector based on a series of tilted-beam images [3, 20], although the measurement accuracy of the coefficients is often within the range of the actual measured values and thus not necessarily useful for this task. Another approach is to look at a feature of an image (*e.g.* the pristine graphene lattice) and find the coefficients which result in the expected appearance for an aberration-free image by trial and error. Other methods for measuring the residual aberrations, *e.g.* from a focus/tilt series [21, 22] or even a single HRTEM image [23] have been presented in the literature.

All the experimental images presented here were acquired using an FEI Titan 80-300 microscope equipped with an image-side hexapole aberration corrector [1]. The microscope was operated at 80 kV and a reduced extraction voltage of 2 kV, in order to reduce the energy spread of the electron beam. The C_s was corrected to $<20\text{ }\mu\text{m}$ and the A_2 and B_2 were corrected to the order of 100 nm (unless stated otherwise).

The graphene samples were produced by the chemical vapor deposition method (acquired commercially from Graphenea S. A.) and transferred on Quantifoil TEM-grids by the procedure described in Ref. [24]. The defect in Figure 1a is produced by carbon deposition, as will be described in detail in a separate paper [25]. The MoSe_2 sample was produced by molecular beam epitaxy and transferred on to Pelco holey silicon nitride TEM grids (a detailed study on this sample will be presented also in a separate article [26]).

The image simulations were conducted using the QSTEM software package [27], using $C_s = 20\text{ }\mu\text{m}$ and focus spread of 6 nm.

3 Results

To verify our approach, we first conducted image simulations, where one has precise control over the aberrations influencing the image. In Figure 2a, a MoSe_2 target with an embedded triangular mirror-domain is simulated with $A_2 = B_2 = 0$. The domain-boundaries are visible, and the lattice inside and outside looks identical except for the reversed order of the darker and brighter appearing sublattices. In order to emulate the effect observed in the experimental image of 1, a HRTEM image was simulated with $A_2 = B_2 = 100\text{ nm}$, and 30° as the azimuthal orientation of both of the aberrations (Figure 2b). With these aberration coefficients the lattice appears completely different inside and outside the mirror-domain. This image was then processed according to equation 4 using the known A_2 and B_2 coefficients, and the resulting image is shown in panel c of Figure 2. The aberration-free appearance of the image is restored by the correction procedure, as predicted.

We also tested the procedure in more extreme conditions, that is, with $A_2 = B_2 = 10\text{ }\mu\text{m}$. This does not represent typical experimental conditions, but should be considered as an artificial test with very strong aberrations. The simulated image is shown in Figure 2d, where the whole image is scrambled by the aberrations and interpretation of the image is practically impossible. However, after applying equation 4 with the known parameters, the image is restored to an aberration-free state. Here, it should be pointed out that the restored image is not perfect, as for example some features can be detected in the vacuum area (which can be attributed to the non-infinite Fourier series in the numerical procedure), but nevertheless the method works even in this extreme situation.

In order to verify our method also in an experimental situation, we took the AC-HRTEM images of figure 1, and applied equation 4. In the case of graphene, we iteratively found the amplitude and orientation of $A_2 = 150\text{ nm}/17^\circ$ which

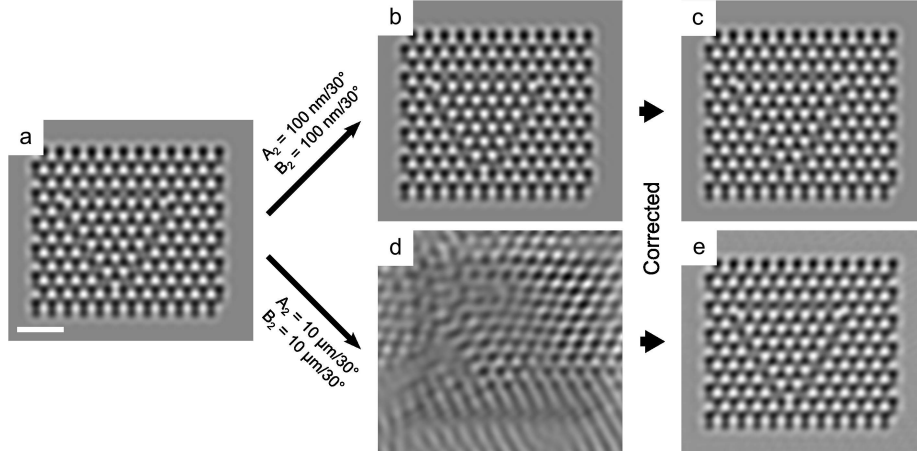


Figure 2: **Simulated verification of the correction procedure.** **a:** A simulated reference HRTEM image of MoSe₂ flake with an embedded mirror domain with zero anti-symmetric aberrations. The same structure simulated with $A_2 = B_2 = 100 \text{ nm}/30^\circ$ (**b**) and $A_2 = B_2 = 10 \mu\text{m}/30^\circ$ (**d**). **c** and **e**: The images of **b** and **d** after applying the correction, with the known parameters. The aberration-free appearance of the image was restored by the method in both cases. The scale bar is 1 nm.

resulted in the removal of visible asymmetry between the two sublattices of graphene. The corrected image is presented in Figure 3a, with the original image shown as inset. The graphene lattice has now the expected hexagonal appearance, and interpretation of the image is straightforward. For the case of MoSe₂, $A_2 = 75 \text{ nm}/15^\circ$ was found to restore the expected appearance of the lattice on both sides of the mirror-twin-boundaries.

An interesting observation in the case of MoSe₂ is that the point defects are actually more visible in one of the domains in the original (non-corrected) image, and also the boundaries are easier to locate due to the different appearances of the lattice on the opposite sides of the boundaries. This is similar to the well known effect of moving away from the 'optimal' Scherzer focus in order to make point defects more visible to the eye (see, *e.g.* Refs. [15, 28]). A clear advantage of exploiting residual anti-symmetric aberrations instead of defocusing is that no information is lost. If the presence of anti-symmetric residual aberrations is deemed beneficial in some situation, our method can just as well be used to *increase* the effect of these aberrations during post-processing.

Another experimental test was conducted by willfully introducing strong A_2 with the corrector of the microscope and acquiring images with such an ill-tuned system ($A_2 = 1.0 \pm 0.1 \mu\text{m}/48^\circ$, as measured by the corrector). In Figure 3 c and d, two locations in the graphene sample are shown. In panel c it is clear that a tilt grain boundary runs through the center of the image, separating two areas with different lattice orientations. However, the atomic structure of the boundary

cannot be interpreted from the image, and the graphene lattice has a completely different appearance on the opposite sides of the boundary (due to different relative orientations of the lattices relative to the A_2 orientation). In panel d, a point defect in the graphene lattice can be detected, but again its structure remains hidden by A_2 . The correction method was applied to both images using the A_2 value of $1\ \mu\text{m}$ at an angle of 41.5° (measured by the corrector) as the starting point, and fine tuning the parameters based on visual inspection of the image. In both cases the effect of A_2 was remedied. In the case of the grain boundary (panel e) a 5-7 dislocation is now visible, as expected for a tilt-grain-boundary in graphene [29, 30, 31, 32]. The structure of the point defect can also now be easily interpreted as a reconstructed divacancy [33]. Moreover, our method offers a much more accurate measurement of the aberration coefficients than what was achievable by the corrector.

4 Conclusion

To conclude, we have presented a method for correcting the anti-symmetric sub-group of aberrations in HRTEM images during numerical post-processing in the case of weak scattering objects. This procedure can be performed on a single conventional HRTEM image, that is, retrieval of the object wave is not necessary. The contribution of the anti-symmetric aberrations is removed by applying the same aberrations with the opposite phase to the Fourier transform of the recorded intensity image and subsequently inverting the Fourier transform, that is, $i_c(\mathbf{x}) = |\mathcal{F}^{-1}\{e^{-i\chi_{as}(\mathbf{u})} \cdot \mathcal{F}\{i_z(\mathbf{x})\}\}|$. We have presented the theoretical justification of the approach. The method was demonstrated on simulated and experimental HRTEM images suffering from residual aberrations (A_2 and B_2). By applying the method, images with strongly reduced aberrations could be produced. In fact, the anti-symmetric aberration coefficients can be freely adjusted *post-situ* using the presented method.

A prerequisite for applying this method is prior knowledge of the aberration coefficients or the expected appearance of the sample in an aberration free image. In the presented examples, the values measured by the corrector were used, or alternatively the coefficients were found by narrowing down the coefficients leading to the correct appearance of the graphene and MoSe_2 lattices through trial and error. The latter approach has an interesting implication: this method can actually be used to *measure* the aberration coefficients when there is prior knowledge on how an aberration-free image should look like. We propose, than an automated algorithm for accurate measurement of residual aberrations can be developed in future work.

The method allows some flexibility during the acquisition of images: As the anti-symmetric residual aberrations can be corrected during post-processing, it is not imperative to have the corrector 'perfectly' tuned at all times. A reasonably good state of correction is important during acquisition, however, in order to enable the operator of the microscope to recognize the imaged features (compare, *e.g.*, Figure 3 d and f). The loosened requirements for the tuning of

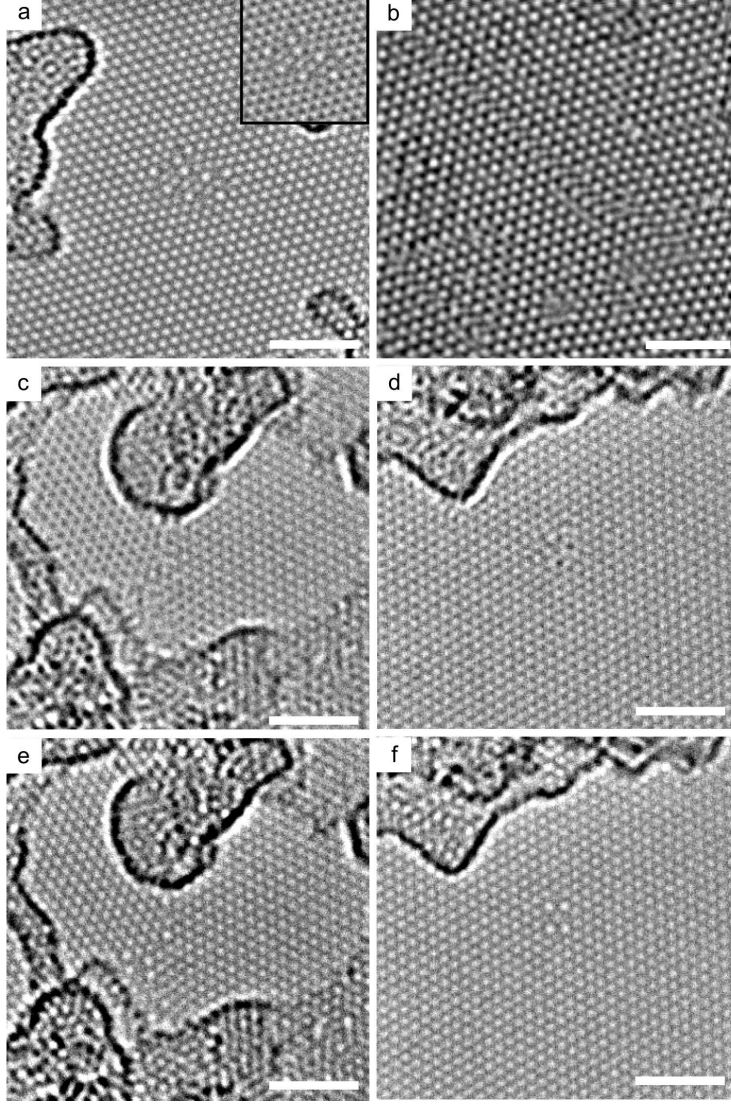


Figure 3: **Experimental verification of the correction method.** **a:** The AC-HRTEM image of Figure 1a after application of the correction method with $A_2 = 150 \text{ nm}/17^\circ$. The hexagonal appearance of the graphene lattice is restored and the structure of the defect is easy to interpret. **b:** The AC-HRTEM image of Figure 1b after the correction method was applied with $A_2 = 75 \text{ nm}/15^\circ$. The MoSe_2 lattice has identical appearance on both sides of the mirror-twin-boundary as expected for an aberration-free image. **c** and **d:** AC-HRTEM images of a tilt grain boundary and a point defect in graphene with A_2 set to $1.0 \pm 0.1 \text{ } \mu\text{m}/48^\circ$ (as measured by the corrector). **e** and **f:** The previous two frames after correcting for $0.9 \text{ } \mu\text{m}/42.5^\circ$ of A_2 and $1.0 \text{ } \mu\text{m}/41.5^\circ$ of A_2 , respectively. In both cases images free of A_2 are recovered and the atomic structure can be interpreted straight-forwardly. The scale bars are 2 nm.

the anti-symmetric aberration coefficients can accelerate the corrector tuning procedure. As the time available for the tuning is limited due to, *e.g.*, gradual drift of the corrector state, an improved final state of correction can be achieved by the faster tuning procedure.

Acknowledgements

We are very grateful to our group member, senior professor Harald H. Rose for invaluable advice during this work. We would also like to thank Hannu-Pekka Komsa and Arkady V. Krashennnikov for helpful discussions, and Niles Vats sample preparation. O.L., D.G., Z.L. and U.K. gratefully acknowledge the funding by the DFG (German Research Foundation) and the Ministry of Science, Research and the Arts (MWK) of Baden-Wuerttemberg in the framework of the SALVE (Sub Angstrom Low-Voltage Electron Microscopy) project. O.L. acknowledges support from the Finnish Cultural Foundation. M.B.W., M.-W.C. and A.K. acknowledge funding from European Research Council (grant no. 240076, FLATRONICS: Electronic devices based on nanolayers)

References

- [1] Haider, M., Rose, H., Uhlemann, S., Schwan, E., Kabius, B. & Urban, K. A spherical-aberration-corrected 200kv transmission electron microscope. *Ultramicroscopy* **75**, 53–60 (1998).
- [2] Scherzer, O. ber einige fehler von elektronenlinsen. *Zeitschrift fr Physik* **101**, 593–603 (1936).
- [3] Uhlemann, S. & Haider, M. Residual wave aberrations in the first spherical aberration corrected transmission electron microscope. *Ultramicroscopy* **72**, 109–119 (1998).
- [4] Meyer, J. C., Kisielowski, C., Erni, R., Rossell, M. D., Crommie, M. F. & Zettl, A. Direct imaging of lattice atoms and topological defects in graphene membranes. *Nano Lett.* **8**, 3582–3586 (2008).
- [5] Krivanek, O. L., Chisholm, M. F., Nicolosi, V., Pennycook, T. J., Corbin, G. J., Dellby, N., Murfitt, M. F., Own, C. S., Szilagy, Z. S., Oxley, M. P., Pantelides, S. T. & Pennycook, S. J. Atom-by-atom structural and chemical analysis by annular dark-field electron microscopy. *Nature* **464**, 571–574 (2010).
- [6] Gabor, D. A new microscopic principle. *Nature* **161**, 777–778 (1948).
- [7] Lichte, H. Electron holography approaching atomic resolution. *Ultramicroscopy* **20**, 293–304 (1986).
- [8] Geiger, D., Lichte, H., Linck, M. & Lehmann, M. Electron holography with a cs-corrected transmission electron microscope. *Microscopy and Microanalysis* **14**, 68–81 (2008).

- [9] Saxton, W. What is the focus variation method? is it new? is it direct? *Ultramicroscopy* **55**, 171–181 (1994).
- [10] Op de Beeck, M., Van Dyck, D. & Coene, W. Wave function reconstruction in hrtem: the parabola method. *Ultramicroscopy* **64**, 167–183 (1996).
- [11] Kirkland, A., Saxton, W., Chau, K.-L., Tsuno, K. & Kawasaki, M. Super-resolution by aperture synthesis: tilt series reconstruction in ctem. *Ultramicroscopy* **57**, 355–374 (1995).
- [12] Coene, W., Thust, A., Op de Beeck, M. & Van Dyck, D. Maximum-likelihood method for focus-variation image reconstruction in high resolution transmission electron microscopy. *Ultramicroscopy* **64**, 109–135 (1996).
- [13] Kirkland, A., Saxton, W. & Chand, G. Multiple beam tilt microscopy for super resolved imaging. *Journal of electron microscopy* **46**, 11–22 (1997).
- [14] Krivanek, O. & Stadelmann, P. Effect of three-fold astigmatism on high resolution electron micrographs. *Ultramicroscopy* **60**, 103 – 113 (1995).
- [15] Meyer, J. C., Kurasch, S., Park, H. J., Skákalová, V., Künzel, D., Groß, A., Chuvilin, A., Algara-Siller, G., Roth, S., Iwasaki, T., Starke, U., Smet, J. H. & Kaiser, U. Experimental analysis of charge redistribution due to chemical bonding by high-resolution transmission electron microscopy. *Nature Mater.* **10**, 209–215 (2011).
- [16] Biskupek, J., Hartel, P., Haider, M. & Kaiser, U. Effects of residual aberrations explored on single-walled carbon nanotubes. *Ultramicroscopy* **116**, 1 – 7 (2012).
- [17] Thust, A., Overwijk, M., Coene, W. & Lentzen, M. Numerical correction of lens aberrations in phase-retrieval {HRTEM}. *Ultramicroscopy* **64**, 249 – 264 (1996).
- [18] Saxton, W. Accurate atom positions from focal and tilted beam series of high resolution electron micrographs. *Scanning Microsc* **2**, 213–224 (1988).
- [19] Ishizuka, K. Phase retrieval from image intensities: Why does exit wave restoration using iwfr work so well? *Microscopy* **62**, S109–S118 (2013).
- [20] Barthel, J. *Ultra-Precise Measurement of Optical Aberrations for Sub-nm Transmission Electron Microscopy*, Ph. D. Thesis (Arizona State University, 2007).
- [21] Meyer, R., Kirkland, A. & Saxton, W. A new method for the determination of the wave aberration function for high resolution tem: 1. measurement of the symmetric aberrations. *Ultramicroscopy* **92**, 89 – 109 (2002).
- [22] Meyer, R., Kirkland, A. & Saxton, W. A new method for the determination of the wave aberration function for high-resolution tem.: 2. measurement of the antisymmetric aberrations. *Ultramicroscopy* **99**, 115 – 123 (2004).

- [23] Stenkamp, D. Detection and quantitative assessment of image aberrations from single hrtem lattice images. *Journal of Microscopy* **190**, 194–203 (1998).
- [24] Algara-Siller, G., Lehtinen, O., Turchanin, A. & Kaiser, U. Dry-cleaning of graphene. *Applied Physics Letters* **104**, 153115 (2014).
- [25] Lehtinen, O., Vats, N., Algara-Siller, G., Knyrim, P. & Kaiser, U. Implantation and atomic scale investigation of self-interstitials in graphene. *arXiv* (2014).
- [26] Lehtinen, O., Komsa, H.-P., Whitwick, M. B., Chen, M.-W., Kis, A., Krashenninnikov, A. V. & Kaiser, U. Microstructure in se-deficient 2d mose₂ (2014). In preparation.
- [27] Koch, C. *Determination of core structure periodicity and point defect density along dislocations*, Ph. D. Thesis (Arizona State University, 2002).
- [28] Lehtinen, O., Tsai, I.-L., Jalil, R., Nair, R. R., Keinonen, J., Kaiser, U. & Grigorieva, I. V. Non-invasive transmission electron microscopy of vacancy defects in graphene produced by ion irradiation. *Nanoscale* **6**, 6569 – 6576 (2014).
- [29] Grantab, R., Shenoy, V. B. & Ruoff, R. S. Anomalous strength characteristics of tilt grain boundaries in graphene. *Science* **330**, 946–948 (2010).
- [30] Yazyev, O. V. & Louie, S. G. Topological defects in graphene: Dislocations and grain boundaries. *Physical Review B* **81**, 195420 (2010).
- [31] Huang, P. Y., Ruiz-Vargas, C. S., van der Zande, A. M., Whitney, W. S., Levendof, M. P., Kevek, J. W., Garg, S., Alden, J. S., Hustedt, C. J., Zhu, Y., Park, J., McEuen, P. L. & Muller, D. A. Grains and grain boundaries in single-layer graphene atomic patchwork quilts. *Nature* **469**, 389–392 (2011).
- [32] Kurasch, S., Kotakoski, J., Lehtinen, O., Skkalov, V., Smet, J., Krill, C. E., Krashenninnikov, A. V. & Kaiser, U. Atom-by-atom observation of grain boundary migration in graphene. *Nano Letters* **12**, 3168–3173 (2012).
- [33] Banhart, F., Kotakoski, J. & Krashenninnikov, A. V. Structural defects in graphene. *ACS nano* **5**, 26–41 (2010).